nature physics

ARTICLES

https://doi.org/10.1038/s41567-019-0728-9

Electrical charging overcomes the bouncing barrier in planet formation

Tobias Steinpilz[1*], Kolja Joeris[1], Felix Jungmann[1], Dietrich Wolf[1], Lothar Brendel[1], Jens Teiser[1], Troy Shinbrot[2] and Gerhard Wurm[1*]

In protoplanetary disks, solid objects (so-called planetesimals) are formed from dust. Micrometre-sized dust grains grow into millimetre-sized aggregates. Once those aggregates have diameters exceeding a few centimetres, they become subject to concentration mechanisms such as the streaming instability, permitting the formation of self-gravitating clusters, which might eventually collapse into kilometre-sized planetesimals. However, for the streaming instability to set in, clumps spanning sizes from centimetres to decimetres are required in the centre of a protoplanetary disk. In the size range between millimetres and centimetres, aggregates bounce off each other rather than sticking together, and growth is stalled. Here we show in microgravity experiments that collisions between millimetre-sized grains lead to sufficient electrical charging for aggregation to bridge this gap between the bouncing barrier and the onset of the streaming instability. We computationally simulate aggregation and find that models agree with the experimental data only if electrical charging is present. We therefore propose that collisional charging may promote early growth in the size gap that current models of planetesimal formation cannot account for.

Current models of terrestrial planet formation start with micrometre-sized dust grains in protoplanetary disks that adhere to each other due to van der Waals and other surface forces. These models are supported by astronomical observations from near-infrared to (sub-)millimetre wavelengths[1]. Substantial numbers of millimetre-sized grains are regularly detected especially at long wavelengths[2,3]. Detection of larger grains is difficult because the surface to mass ratio decreases with increasing grain size; however, millimetre-sized grains are abundant in primitive meteorites. A large proportion of chondrites also consist of millimetre-sized, almost spherical granules, giving this size a special importance[4,5].

Particle aggregation has also been extensively investigated in theoretical and computational studies, invariably confirming the finding that beyond the millimetre size, particles tend to bounce off one another rather than aggregate[6–8]. Growth beyond this so-called bouncing barrier can be promoted by larger seeds, but even in the presence of such seeds, millimetre-sized aggregates would predominate[9,10]. Moreover, a second, 'fragmentation' barrier associated with aggregate destruction by high-mass, high-kinetic-energy collisions limits aggregate sizes to centimetres or below[11].

To account for the simple fact that asteroids and planets do exist, several possible mechanisms have been investigated for growth beyond the millimetre scale. Streaming and other resonant drag instabilities have been shown to regulate the concentration of particles, permitting formation of self-gravitating clumps that can ultimately collapse into kilometre-sized planetesimals[12–16]. Streaming instabilities, however, require a minimum particle size of centimetres to decimetres in the inner few astronomical units of a protoplanetary disk[13,17,18]. Numerical studies to better refine the minimum aggregate size at which streaming instabilities operate are ongoing; however, these analyses indicate that sub-centimetre-sized particles cannot be concentrated to the point of gravitational collapse in the inner protoplanetary disk[19].

Ground-based and microgravity experiments also confirm the presence of a bouncing barrier: in those experiments, millimetre-sized aggregates compact and stop growing at collision velocities well below the $1\,\mathrm{m\,s^{-1}}$ expected in protoplanetary disks close to 1 AU (refs. [20–25]).

In summary, astronomical observations, theory, simulations and experiments on early planet formation all agree that there should be a gap of one or two orders of magnitude in aggregate size separating sub-millimetre and super-centimetre scales.

One mechanism that might bridge this gap is electrostatic attraction. Experiments show that granular collisions generate oppositely charged grains, even when grains are identical[26–30]. Recent proposals for the understanding of collisional electrical charging have also been advanced[31,32], and collisional charging of millimetre-sized grains has been studied from several perspectives. For example, the problem of lightning generation in protoplanetary disks and terrestrial dust storms has been examined[33–36].

We focus analysis here on the bouncing barrier, which involves collisions between millimetre-sized particles. Other work on related topics is also notable, however. First, charge-mediated aggregation of smaller grains than we consider here has been observed: micrometre-sized dust grains can rapidly aggregate in microgravity[37], with no apparent large-scale cutoff. Second, Jungmann and colleagues[29] demonstrated that charging of half-millimetre glass grains can increase the collision velocity below which sticking occurs by more than an order of magnitude. Third, mechanisms of aggregation by charged particles have been studied theoretically. In particular, Feng[38] found that even two spheres with same sign charge can attract if one charge is substantially larger than the other, and Matias and colleagues[39] classified particle charges that can hold aggregates of numerous dielectric particles together.

Motivated both by this recent progress in understanding collisional charging and the longstanding need for improved knowledge of planetesimal growth through the bouncing barrier, we investigate here whether collisional charging of identical, chondrule-sized (sub-millimetre) grains promotes the formation of large multiparticle aggregates under conditions of microgravity.

[1]Faculty of Physics, University of Duisburg-Essen, Duisburg, Germany. [2]Department of Biomedical Engineering, Rutgers University, Piscataway, NJ, USA.
*e-mail: tobias.steinpilz@uni-due.de; gerhard.wurm@uni-due.de

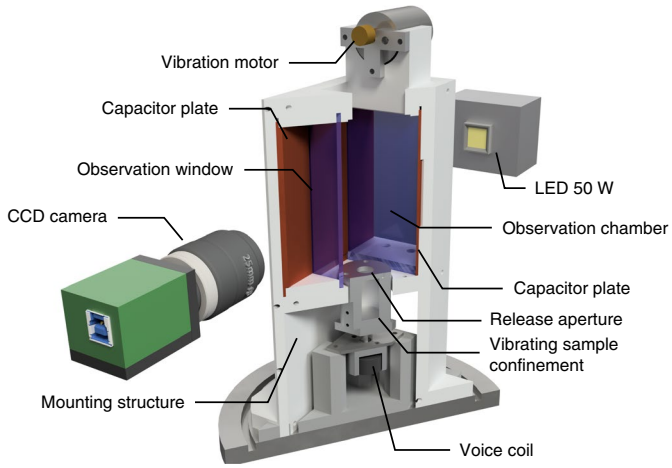

Fig. 1 | Sketch of the apparatus used in microgravity. Charged grains are released from below (in this view) into the observation chamber, where they are photographed at 180 f.p.s., 75 μm pixel^{-1}.

Microgravity experiments

To quantify aggregation associated with collisional charging, we carried out microgravity experiments in the Bremen drop tower. A sketch of the apparatus is shown in Fig. 1 (see Methods for experimental details).

We used glass spheres in these experiments, because they are readily available with nearly identical size and material. In all of these experiments, we perform the following sequence of procedures (details in Methods).

Pre-flight procedures. The experimental apparatus is sealed in a gas-tight chamber with CO_2 at around 1,050 mbar and flushed (evacuated to less than 0.2 mbar) twice before the experimental trials. The particle reservoir is vibrated for at least 10 min immediately before microgravity launch. Separate experiments in our laboratory confirm that an equilibrium charge distribution is established within 10 min and persists over several hours.

In-flight procedures. The apparatus in Fig. 1 is launched and remains weightless for 9 s. At the onset of microgravity, grains exit the shaker through an aperture into an observation chamber, where they are photographed at 180 f.p.s. with spatial resolution of 75 μm per pixel. Figure 2a displays a typical frame showing both aggregates and individual grains.

The observation chamber is sandwiched between two capacitor plates that are attached to a high-voltage supply. The resulting electric field accelerates charged particles, permitting measurement of the charge to mass ratio.

Experimental data. Data gathered from video frames are used to evaluate aggregate size and particle charge. The masses of the grains are identical and easily measured, and trajectories of individual particles are used to evaluate their net charge in the standard way. The resulting charge distribution for glass spheres is shown in Fig. 3: this distribution looks similar in all experiments analysed. Notably, Haeberle and colleagues[40] recently showed that stochastic charging and discharging can be expected to generate a two-exponential distribution, and we fit this prediction to our data in Fig. 3.

We find that charging leads to effective aggregation on multiple size scales.

At the smallest scales, individual grains are seen to form dimers, trimers and clusters of several grains (see Methods).

At moderate scales, aggregates of countable grains (tens to hundreds) are also evident—size distributions of these are shown in Fig. 4 (black dots). The raw data of the three individual experiments that were added together and binned to generate Fig. 4 are shown in Extended Data Fig. 8.

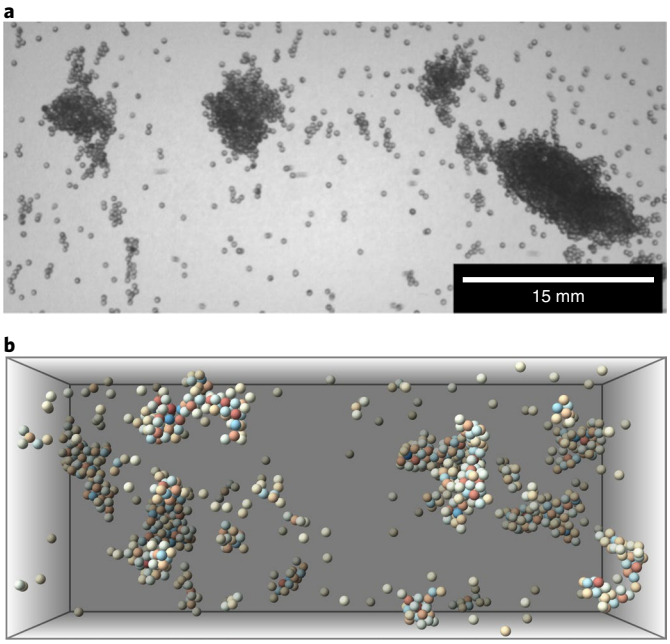

Fig. 2 | Aggregates in experiment and simulation. a, Aggregates emerging from the shaker under microgravity can be up to several centimetres in size (for experimental parameters see Table 1). **b**, Simulated aggregates formed within the shaker.

Our simulations indicate that particle charges probably form such aggregates within the shaker; comparative distributions from the simulations (also shown in Fig. 2b), are discussed in the next section.

At larger scales, centimetre-sized aggregates also form, as shown in Fig. 2a. It is not possible to count these particles because the front monolayer obscures particles behind, but estimates assuming comparable width and depth indicate that they consist of over a thousand grains.

At all scales, aggregates seem to be robust: although very high speed impacts can sometimes lead to disintegration (see Extended Data Fig. 4), aggregates typically remain intact following collision with the wall or with individual grains moving well beyond the fragmentation limit of uncharged aggregates (>10 cm s^{-1}; see Extended Data Fig. 7 and Supplementary Video 2).

Numerical simulations

The cloud of particles within the shaker is too dense to permit observations of aggregates as they form, so the experimental data are measurements of clusters formed in the shaker and expelled through the aperture. To assess aggregate formation itself, we therefore simulated collisions and compared the experimental and simulated aggregate size distributions with and without electrostatic effects. The simulations compact and then release 10,000 grains subject to standard contact mechanics methods, to which we can add Coulomb forces due to charged particles (details provided in Methods).

Typical simulated clusters are shown in Fig. 2b, and distributions of aggregates' sizes with and without Coulomb forces are shown in Fig. 4. The simulation data are binned to reduce scatter: the logarithmic abscissa is subdivided into equally sized bins and sets of data points within each bin are replaced by one point at the set's centre of mass. The experimental data are thus sums, and error bars show

Table 1 | List of the experiments and corresponding parameters used for the figures

Fig.	Extended Data Figs.	Experiment ID	U_{Cap}	T_{Shake}	D	Shaker material
			(kV m^{-1})	(min)	(mm)	
2		C1A1	42	10	10	Glass beads
3	1, 4	C1A2	42	10	5	Glass beads
4	4, 8	C3A1, C3A6	83	15	5	Glass beads
4	8	C3A3	83	15	5	Aluminium

Fig. 4 combines our data from three experiments: no statistically significant difference is found in cluster sizes due to capacitor voltage or shaker material. All samples consist of 434 μm glass beads and are carried out under a CO_2 atmosphere. U_{Cap}, capacitor voltage; T_{Shake}, shaking duration; D, aperture diameter.

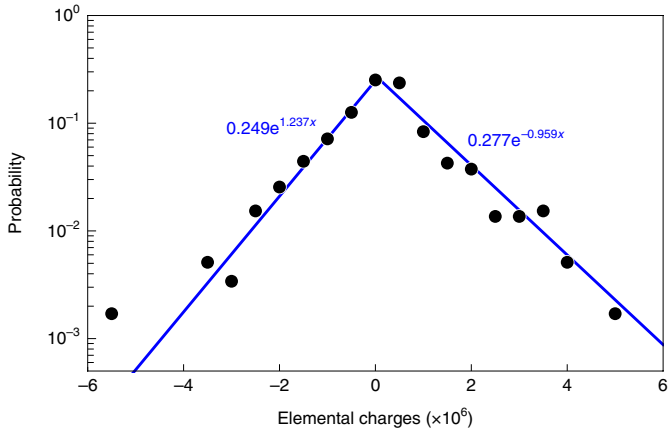

Fig. 3 | Charge distribution of individual grains. Black dots show a histogram of grain charges from the experiment shown in Extended Data Fig. 1 (parameters recorded in Table 1, grain properties shown in Extended Data Figs. 2 and 3). The uncertainties in the charge measurements are 15%. Blue lines are exponential fits, as predicted by Haeberle and colleagues[40]. The specific parameters for the fits are shown next to the lines.

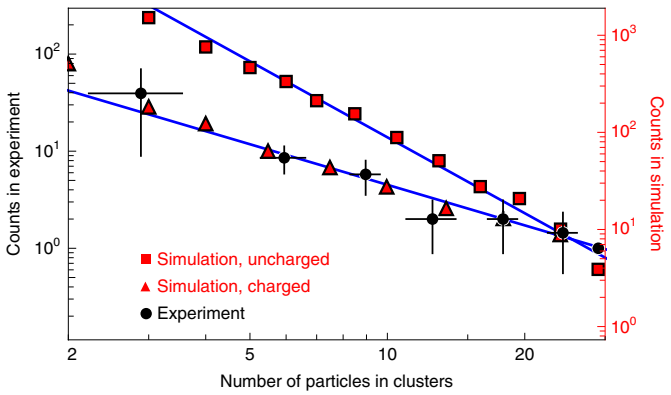

Fig. 4 | Size distributions of moderate-sized clusters. Clusters from the simulations of uncharged and charged grains are shown in red. The scale for the absolute number of clusters in the numerical simulations is on the right y axis. The blue lines are power law fits to the simulation data with slopes of -1.39 ± 0.08 for the charged grains and -2.6 ± 0.1 for the uncharged case. Clusters from the experiments are shown in black. The scale for the absolute number of clusters in the experiments is on the left y axis. Experimental data (for parameters see Table 1) are summed from three individual trials and averaged. Error bars for the experiments are standard deviations. For raw experimental data of each trial see Extended Data Fig. 8.

corresponding standard deviations. Fitting uses the raw, unbinned data (also shown in Fig. 4), and we exclude monomers as well as very large clusters that are too rare to be statistically meaningful.

Our comparative experimental results in Fig. 4 show data from three independent trials (for the experimental parameters used to create the figures see Table 1). The experiments produce fewer measurable aggregates than the simulations, so we bin the experimental data as with the simulations to improve statistical reliability, but plot the geometric mean of the data from three adjacent points. Monomers are again excluded.

Both the experimental and simulated data in the presence of electrostatics produce size distributions described by a power law $N(n) \propto n^m$ with slope $m = -1.39 \pm 0.08$. The simulations with uncharged grains, however, produce fewer large clusters and so generate a steeper slope, $m = -2.6 \pm 0.1$. Power law behaviour is expected in scale-free processes such as aggregation[41,42], but the slope depends on specifics of the problem.

Broadly speaking, slopes shallower than about −1.5 tend to be associated with dense and deformable clusters[43], and are expected to result from slow processes such as electrostatics, where aggregation involves repeated interactions[44]. Indeed, in our experiments charged particles do repeatedly orbit and collide with one another before sticking (see Extended Data Fig. 6 and Supplementary Video 1), and large-scale aggregates are observed to be dense and deformable (see Extended Data Fig. 7 and Supplementary Video 2). By contrast, steeper slopes are associated with fewer large clusters, and are expected for rapid, contact-mediated processes[45]—again in agreement with our findings.

Based on existing literature, our results therefore seem to be consistent with the proposition that particle aggregation in microgravity is dominated by electrostatics, and not by contact-mediated influences. To confirm that the shallow slopes seen in Fig. 4 are not instead produced by other mechanisms than electrostatics, we performed additional sets of simulations. Specifically, we varied the simulated compression acting on grains by increasing the catapult acceleration up to 50 times the gravitational acceleration, and we increased contact cohesion between particles up to 30 times the gravitational force that would act on a grain on ground. However, we were unable to reproduce the shallow experimental scaling in any of these simulations without including particle charges.

Application to protoplanetary disks

The collision velocities in the experiments are between millimetres and metres per second: in the range of typical velocities for millimetre- to centimetre-sized particles in protoplanetary disks around 1 AU (refs. [8,20]). At the low particle densities expected to be present there, Zsom and colleagues[8] find that dust aggregates larger than about 1 mm do not aggregate, but bounce off one another. Indeed, uncharged aggregates disintegrate at as little as a few millimetres per second (ref. [24]), while our experiments involving charged grains produce growth of aggregates at speeds up to a few decimetres per second, and are only destroyed at the highest speeds encountered (a few metres per second). We conclude that collisions

between chondrule-sized particles in a velocity range found in protoplanetary disks can produce aggregates of several centimetres in size provided that the particles are electrically charged. Thus, it is apparently possible for collisional charging to transform bouncing millimetre-sized grains into growing centimetre-sized aggregates. Whether this occurs depends on the relative rates of material charging versus discharging, and particle collisions versus dispersal. It is evident that unravelling the details of relations between charging and aggregation in protoplanetary disks will require considerable additional study.

Notwithstanding this caveat, we remark that depending on the location and local particle density within a protoplanetary disk, other charge mechanisms could augment collisional charging. For example, charging in a plasma generated by cosmic radiation, and charging by the decay of radioactive ^{26}Al or ^{40}K have been discussed as possible mechanisms (see Methods and Okuzumi[46], Matthews and colleagues[47], Johansen and Okuzumi[48], and Bergin and colleagues[49]).

Moreover, the data we report here involved pure glass spheres. Particles in protoplanetary disks are mixtures of silicates, and to mimic these we performed additional trials using basalt spheres: we find that these charge an order of magnitude more strongly than glass spheres of similar size. Basalt contains numerous different minerals, each of which could potentially complicate charging effects, and so the details of how these materials affect charging and aggregation remain unclear. Nevertheless, the finding that basalt charges much more strongly than glass, confirmed by ground-based charge measurements in our laboratory, suggests that our reported data may provide a conservative estimate of electrostatic influences on aggregation in protoplanetary disks.

Online content

Any methods, additional references, Nature Research reporting summaries, source data, extended data, supplementary information, acknowledgements, peer review information; details of author contributions and competing interests; and statements of data and code availability are available at https://doi.org/10.1038/s41567-019-0728-9.

Received: 22 November 2018; Accepted: 18 October 2019;
Published online: 09 December 2019

References

1. Testi, L. et al. in *Protostars and Planets VI* (eds Beuther, H. et al.) 339–362 (Univ. Arizona Press, 2014).
2. Pohl, A. et al. The circumstellar disk HD 169142: gas, dust, and planets acting in concert? *Astrophys. J.* **850**, 52 (2017).
3. Pinilla, P. et al. A multi-wavelength analysis of dust and gas in the SR 24S transition disk. *Astrophys. J.* **839**, 99 (2017).
4. Weisberg, M. K., McCoy, T. J. & Krot, A. N. in *Meteorites and the Early Solar System II* (eds Lauretta, D. S. & McSween, H. Y. Jr) 19–52 (Univ. Arizona Press, 2006).
5. Friedrich, J. M. et al. Chondrule size and related physical properties: a compilation and evaluation of current data across all meteorite groups. *Geochemistry* **75**, 419–443 (2015).
6. Dominik, C. & Tielens, A. G. G. M. The physics of dust coagulation and the structure of dust aggregates in space. *Astrophys. J.* **480**, 647–673 (1997).
7. Tanaka, H., Wada, K., Suyama, T. & Okuzumi, S. Growth of cosmic dust aggregates and reexamination of particle interaction models. *Prog. Theor. Phys. Suppl.* **195**, 101–113 (2012).
8. Zsom, A., Ormel, C. W., Güttler, C., Blum, J. & Dullemond, C. P. The outcome of protoplanetary dust growth: pebbles, boulders, or planetesimals? II. Introducing the bouncing barrier. *Astron. Astrophys.* **513**, A57 (2010).
9. Windmark, F. et al. Planetesimal formation by sweep-up: how the bouncing barrier can be beneficial to growth. *Astron. Astrophys.* **540**, A73 (2012).
10. Booth, R. A., Meru, F., Lee, M. H. & Clarke, C. J. Breakthrough revisited: investigating the requirements for growth of dust beyond the bouncing barrier. *Mon. Not. R. Astron. Soc.* **475**, 167–180 (2018).
11. Birnstiel, T., Ormel, C. W. & Dullemond, C. P. Dust size distributions in coagulation/fragmentation equilibrium: numerical solutions and analytical fits. *Astron. Astrophys.* **525**, A11 (2011).
12. Youdin, A. N. & Goodman, J. Streaming instabilities in protoplanetary disks. *Astrophys. J.* **620**, 459–469 (2005).
13. Johansen, A. et al. in *Protostars and Planets VI* (eds Beuther, H. et al.) 547–570 (Univ. Arizona Press, 2014).
14. Simon, J. B., Armitage, P. J., Li, R. & Youdin, A. N. The mass and size distribution of planetesimals formed by the streaming instability. I. the role of self-gravity. *Astrophys. J.* **822**, 55 (2016).
15. Schreiber, A. & Klahr, H. Azimuthal and vertical streaming instability at high dust-to-gas ratios and on the scales of planetesimal formation. *Astrophys. J.* **861**, 47 (2018).
16. Squire, J. & Hopkins, P. F. Resonant drag instabilities in protoplanetary discs: the streaming instability and new, faster growing instabilities. *Mon. Not. R. Astron. Soc.* **477**, 5011–5040 (2018).
17. Bai, X.-N. & Stone, J. M. Dynamics of solids in the midplane of protoplanetary disks: implications for planetesimal formation. *Astrophys. J.* **722**, 1437–1459 (2010).
18. Drazkowska, J. & Dullemond, C. P. Can dust coagulation trigger streaming instability? *Astron. Astrophys.* **572**, A78 (2014).
19. Yang, C.-C., Johansen, A. & Carrera, D. Concentrating small particles in protoplanetary disks through the streaming instability. *Astron. Astrophys.* **606**, A80 (2017).
20. Weidenschilling, S. J. & Cuzzi, J. N. in *Protostars and Planets III* (eds Levy, E. H. & Lunine, J. I.). 1031–1060 (Univ. Arizona Press, 1993).
21. Blum, J. & Wurm, G. The growth mechanisms of macroscopic bodies in protoplanetary disks. *Annu. Rev. Astron. Astrophys.* **46**, 21–56 (2008).
22. Weidling, R., Güttler, C., Blum, J. & Brauer, F. The physics of protoplanetesimal dust agglomerates. III. Compaction in multiple collisions. *Astrophys. J.* **696**, 2036–2043 (2009).
23. Güttler, C., Blum, J., Zsom, A., Ormel, C. W. & Dullemond, C. P. The outcome of protoplanetary dust growth: pebbles, boulders, or planetesimals? I. Mapping the zoo of laboratory collision experiments. *Astron. Astrophys.* **513**, A56 (2010).
24. Kelling, T., Wurm, G. & Koester, M. Experimental study on bouncing barriers in protoplanetary disks. *Astrophys. J.* **783**, 111 (2014).
25. Demirci, T. et al. Is there a temperature limit in planet formation at 1000 K? *Astrophys. J.* **846**, 48 (2017).
26. Méndez Harper, J. & Dufek, J. The effects of dynamics on the triboelectrification of volcanic ash. *J. Geophys. Res. Atmos.* **121**, 8209–8228 (2016).
27. Waitukaitis, S. R., Lee, V., Pierson, J. M., Forman, S. L. & Jaeger, H. M. Size-dependent same-material tribocharging in insulating grains. *Phys. Rev. Lett.* **112**, 218001 (2014).
28. Yoshimatsu, R., Araújo, N. A. M., Wurm, G., Herrmann, H. J. & Shinbrot, T. Self-charging of identical grains in the absence of an external field. *Sci. Rep.* **7**, 39996 (2017).
29. Jungmann, F., Steinpilz, T., Teiser, J. & Wurm, G. Sticking and restitution in collisions of charged sub-mm dielectric grains. *J. Phys. Commun.* **2**, 095009 (2018).
30. Lee, V., James, N. M., Waitukaitis, S. R. & Jaeger, H. M. Collisional charging of individual submillimeter particles: using ultrasonic levitation to initiate and track charge transfer. *Phys. Rev. Mater.* **2**, 035602 (2018).
31. Lacks, D. J. & Sankaran, R. M. Contact electrification of insulating materials. *J. Phys. D* **44**, 453001 (2011).
32. Siu, T., Cotton, J., Mattson, G. & Shinbrot, T. Self-sustaining charging of identical colliding particles. *Phys. Rev. E* **89**, 052208 (2014).
33. Desch, S. J. & Cuzzi, J. N. The generation of lightning in the solar nebula. *Icarus* **143**, 87–105 (2000).
34. Muranushi, T. Dust-dust collisional charging and lightning in protoplanetary discs. *Mon. Not. R. Astron. Soc.* **401**, 2641–2664 (2010).
35. Pähtz, T., Herrmann, H. J. & Shinbrot, T. Why do particle clouds generate electric charges? *Nat. Phys.* **6**, 364–368 (2010).
36. Wurm, G., Schmidt, L., Steinpilz, T., Boden, L. & Teiser, J. A challenge for Martian lightning: limits of collisional charging at low pressure. *Icarus* **331**, 103–109 (2019).
37. Konopka, U. et al. Charge-induced gelation of microparticles. *New J. Phys.* **7**, 227 (2005).
38. Feng, J. Q. Electrostatic interaction between two charged dielectric spheres in contact. *Phys. Rev. E* **62**, 2891–2897 (2000).
39. Matias, A. F. V., Shinbrot, T. & Araújo, N. A. M. Mechanical equilibrium of aggregates of dielectric spheres. *Phys. Rev. E* **98**, 062903 (2018).
40. Haeberle, J., Schella, A., Sperl, M., Schröter, M. & Born, P. Double origin of stochastic granular tribocharging. *Soft Matter* **14**, 4987–4995 (2018).
41. Corral, Á. & González, Á. Power law size distributions in geoscience revisited. *Earth Space Sci.* **6**, 673–697 (2019).
42. Lin, M. Y. et al. Universality in colloid aggregation. *Nature* **339**, 466–469 (1989).
43. Meakin, P. & Family, F. Structure and dynamics of reaction-limited aggregation. *Phys. Rev. A* **36**, 5498–5501 (1987).
44. Meakin, P. Aggregation kinetics. *Phys. Scripta* **46**, 295–331 (1992).
45. Ball, R. C., Weitz, D. A., Witten, T. A. & Leyvraz, F. Universal kinetics in reaction-limited aggregation. *Phys. Rev. Lett.* **58**, 274–277 (1987).

46. Okuzumi, S. Electric charging of dust aggregates and its effect on dust coagulation in protoplanetary disks. *Astrophys. J.* **698**, 1122–1135 (2009).
47. Matthews, L. S., Shotorban, B. & Hyde, T. W. Cosmic dust aggregation with stochastic charging. *Astrophys. J.* **776**, 103 (2013).
48. Johansen, A. & Okuzumi, S. Harvesting the decay energy of ^{26}Al to drive lightning discharge in protoplanetary discs. *Astron. Astrophys.* **609**, A31 (2018).
49. Bergin, E. A., Aikawa, Y., Blake, G. A. & van Dishoeck, E. F. in *Protostars and Planets V* (eds Reipurth, B. et al.) 751–766 (Univ. Arizona Press, 2007).

Methods

Drop tower experiments. The experiments were carried out in the Bremen drop tower, in which the apparatus shown in Fig. 1 is launched by a catapult producing 9 s with residual acceleration of less than $1\times10^{-5}g$. We describe five resulting microgravity experiments in the present work, itemized in Table 1.

The container for shaking the grains is cylindrical with a diameter of 20 mm and height of 25 mm. The cylinder and lids are constructed of aluminium, creating a Faraday cage around the sample. We used monodisperse 434 µm diameter glass spheres in our experiments, and in all experiments but one (see Table 1), the same spheres as used in each experiment are glued to the insides of the lids and cylinder, preventing grains from contacting a different material, and producing grains with minimal charge bias. To test for the effect of bias, in one experiment no spheres were glued to the inside of the shaker: we detected no resulting difference in cluster sizes, however.

As described earlier, particles were vibrated for at least 10 min before launch by the voice coil shown in Fig. 1. After launch, the removal of gravity releases the grains toward the lid, causing particles to emerge into the observation volume. We also vibrated the shaker during microgravity to launch fast grains in separate collisional experiments shown in Supplementary Video 2. In further experiments, a second vibration motor on top of the experiment was activated to vibrate the entire capacitor and so detach adhered particles. In this way, we measured charging of grains at each electrode; these experiments show that rebounding collisions (short contact time with electrode) only weakly affect particle charges (see subsection 'Glass sphere sample' below).

For observation we used bright field illumination and a camera recording at 180 fps and a spatial resolution of 75 µm pixel^{-1}, which is sufficient to resolve individual grains as well as to visualize the entire observation volume of $90\times48\times36\,\mathrm{mm}^3$.

The electrical field applied to the capacitor was varied from 0 to 83 kV m^{-1}. Higher d.c. voltages were used to separate and measure particle charges (as presented) and lower voltages were used for aggregation studies.

At the highest electric field strengths, aggregates can impact the walls with a velocity beyond the fragmentation limit. In these cases, the charge of the constituent grains of a cluster can be evaluated from trajectories following fragmentation (exemplar shown in Extended Data Fig. 4a).

Image analysis. Extended Data Fig. 1 shows trajectories of grains produced by superimposing 180 individual images. A small aperture was used for this photo to show individual trajectories with few aggregates. Detailed image analysis was carried out using ImageJ 1.52[50] to obtain individual particle positions. Trajectories of grains were then fitted with parabolas, providing accelerations of grains approaching the capacitor plates. Since all grains are identical, the mass of each grain is known and measured accelerations can be used to obtain the grain charges shown in Fig. 3.

Glass sphere sample. An example image of the glass spheres used in the experiments reported here is shown in Extended Data Fig. 2 and a measured size distribution is given in Extended Data Fig. 3.

To assess electrostatic forces holding aggregates together, we must evaluate the charges on each grain within an aggregate. Fortunately, as mentioned earlier, these can be measured following fragmentation events: if an aggregate has a net charge, it can be accelerated to collide with a capacitor wall at high speed, sometimes resulting in disintegration, as shown in Extended Data Fig. 4a. The charges of individual grains can then be evaluated from their rebounding trajectories (shown also in Extended Data Fig. 1).

We note that this procedure assumes that little charge is exchanged by contact between grains and the wall. This was confirmed by analysis of individual grain–wall collisions, which show that the median charge transfer in a wall collision is about 27,000 elementary charges: an order of magnitude lower than the net grain charges measured in experiments[29].

Two aggregates that are observed to disintegrate after contact with the wall are shown in Extended Data Fig. 4b,c, with absolute charges attributed to each grain. Also shown in Extended Data Fig. 4a are trajectories of a fragmenting aggregate.

Aggregates that collide with container walls sufficiently energetically to disintegrate must have substantial net charge, and this is seen in the examples shown in Extended Data Fig. 4b,c. The aggregate in Extended Data Fig. 4c in particular appears to be composed only of grains with the same sign (see Feng[38] and Matias and colleagues[39]). This indicates that collisional charging may produce significant multipolar variations in charge within single particles.

Collisions and aggregation. In several cases, Kepler orbits of charged particles are visible (similar to Lee and colleagues[51]). Extended Data Fig. 6 shows a sequence of dimer formation with two grains colliding, bouncing and sticking to each other at 5.4 mm s^{-1}—the whole collision can also be found in Supplementary Video 1. Supplementary Video 3 shows the formation of an aggregate consisting of 7 grains.

Extended Data Fig. 7 shows three images of the impact of an individual grain with 0.13 m s^{-1} into a larger aggregate. The aggregate deforms but does not break—shown in more detail in Supplementary Video 2.

According to Dominik and Tielens[6], the impact energy before a particle is lost should be about $E_l = 0.3 n_c E_{break}$, where n_c is the total number of contacts in the aggregate and $E_{break} = 43\frac{\gamma^{5/3}R^{4/3}}{E^*}$, for surface energy $\gamma = 0.3\,\mathrm{J\,m^{-2}}$ (already an overestimate for perfectly smooth spheres), grain radius $R = 217$ µm and $E^* = \frac{E}{2(1-\nu^2)}$ with the Poisson ratio $\nu \approx 0$ and Young's modulus $E = 6\times10^{10}$ Pa. For an estimated $n_c = 100$ we get $E_l = 10^{-13}$ J. This is equivalent to an impact velocity of about 1 mm s^{-1}. The individual grain impacts with an energy $E = 10^{-8}$ J, which is orders of magnitude larger. In fact this should lead to catastrophic disruption ($E_l = 10 n_c E_{break}$) as the measured energy is also orders of magnitude beyond that critical value.

***N*-body simulations.** As we have mentioned, the density of grains in the shaker is too high to permit observation of aggregate formation, so we investigated that process with discrete element simulations using the LIGGGHTS 3.7.0 software package[52]. We include all rotational and translational degrees of freedom and simulate 10,000 spherical particles of mass $m = 10^{-6}$ kg and diameter $d = 425$ µm.

To calculate contact forces we chose a dissipative Hertzian model as described by Kuwabara and Kono[53]. A short range attraction is included by means of a simplified Johnson–Kendall–Roberts model, in which the force between grains i and j is of the form $F_{ij,\mathrm{coh}} = \gamma_s A_{ij}$, with a surface energy density γ_s and contact area A_{ij}. For small overlaps the contact area is simplified to $A_{ij} \approx \pi\delta_{ij}d$, where δ_{ij} is the particle diameter. This is implemented in LIGGGHTS under the keyword SJKR2.

Mechanical properties used are the restitution coefficient $e = 0.982$, $\nu = 0.2$, $E = 500$ kPa and $\gamma_s = 2\,\mathrm{mJ\,m^{-3}}$. The small value of E was chosen to improve computational efficiency, and γ_s was calibrated to agree with measured values[54].

Each particle was assigned a central charge q taken randomly from a Gaussian distribution with mean $\mu = 0$ and standard deviation σ. Charge inhomogeneities within each particle are not considered in this work. The simulations were conducted for several values of σ: for Fig. 4 we used $\sigma = 10^6\,e$ *(e, elementary charge)*, because smaller values had no observable impact on cluster statistics, and larger values tended to produce clusters larger than can be observed in the experiments.

To account for image charges at the bottom boundary (see simulation domain below), each grain's charge and position is mirrored at that plane. The Coulomb interaction between grains or their image charges is calculated directly, with a cutoff for distances larger than $d_{cut} \approx 3.5$ mm. Separate simulations reveal that the inner structure and statistical distribution of clusters are unchanged by increasing the cutoff value.

The simulation domain measures 10 mm in the lateral directions, and periodic horizontal boundary conditions are employed, meaning that the system acts as if it were surrounded by copies of itself in an infinite crystal lattice. In the vertical direction, the box is bounded by a bottom conducting plate, and is tall enough to not restrict particle movement above. The 10,000 grains are assigned random initial velocities and positions, and each simulation is conducted ten times with newly assigned charges, positions and speeds drawn from the same distributions.

At the beginning of each simulation, Earth's gravity acts on every particle. After all particles have settled (Extended Data Fig. 5a), the catapult's acceleration is added, which in total is ten times the gravitational acceleration. After oscillations induced by this step have stopped, the catapult force and gravity are turned off and the sediment relaxes and disintegrates into fragments that can form clusters, as shown in Extended Data Fig. 5b.

The expansion lasts for 9 s as in the drop tower experiments, and the resulting cluster size distributions for charged and uncharged grains are analysed and plotted in Fig. 4 as we have described.

Cosmic radiation versus collisional charging. Cosmic radiation and radioactive decay can ionize gas molecules in protoplanetary disks, producing electrons and ions[49]. These can charge or discharge grains and thus compete with contact charging. Here, we estimate their impact. Typical values found in the literature for ionization rates in the dense midplane of protoplanetary disks are of the order of $\zeta = 10^{-23}$ ions per gas molecule per second[49,55,56]. Considering a gas density of 1 mg m^{-3} or equivalently a molecule number density of about $n_g = 10^{20}\,\mathrm{m^{-3}}$, this amounts to a creation rate of $p = n_g\zeta = 10^{-3}\,\mathrm{s^{-1}\,m^{-3}}$—that is, one charge pair per m^3 in 1,000 s. Regarding dust, we assume a solid to gas mass ratio of 1 as, for example, expected after sedimentation of solids to the disk midplane. For dust particles of about 0.1 mg, this means a number density of $n = 10\,\mathrm{m^{-3}}$. With a geometrical cross section of $\sigma \approx 10^{-6}\,\mathrm{m^2}$ and a typical relative velocity of $v \approx 0.1\,\mathrm{m\,s^{-1}}$, this allows us to estimate the average time between collisions as $\tau = \frac{1}{n\sigma v} \approx 10^6$ s.

During this time, a particle can encounter at most $\tau p/n = 10^3$ elementary charges created by ionizing radiation, which is two orders of magnitude below the 10^5 elementary charges that are on average transferred during a collision of two particles.

Data availability

The data represented in Figs. 3 and 4 and in Extended Data Figs. 3 and 8 are available with the online version of this paper. All other data that supports the plots within this paper and other findings of this study are available from the corresponding authors on reasonable request.

Code availability

The code for the numerical simulation is available from the corresponding authors on reasonable request.

References

50. Schneider, C. A., Rasband, W. S. & Eliceiri, K. W. NIH Image to ImageJ: 25 years of image analysis. *Nat. Methods* **9**, 671–675 (2012).
51. Lee, V., Waitukaitis, S. R., Miskin, M. Z. & Jaeger, H. M. Direct observation of particle interactions and clustering in charged granular streams. *Nat. Phys.* **11**, 733–737 (2015).
52. Kloss, C., Goniva, C., Hager, A., Amberger, S. & Pirker, S. Models, algorithms and validation for opensource DEM and CFD-DEM. *Prog. Comput. Fluid Dynam.* **12**, 140–152 (2012).
53. Kuwabara, G. & Kono, K. Restitution coefficient in a collision between two spheres. *Japan. J. Appl. Phys.* **26**, 1230–1233 (1987).
54. Demirci, T. et al. Are pebble pile planetesimals doomed? *Mon. Not. R. Astron. Soc.* **484**, 2779–2785 (2019).
55. Cleeves, L. I., Adams, F. C. & Bergin, E. A. Exclusion of cosmic rays in protoplanetary disks: stellar and magnetic effects. *Astrophys. J.* **772**, 5 (2013).
56. Kataoka, R. & Sato, T. Ionization of protoplanetary disks by galactic cosmic rays, solar protons, and supernova remnants. *Geosci. Front.* **8**, 247–252 (2017).

Acknowledgements

This project is supported by DLR Space Administration with funds provided by the Federal Ministry of Economic Affairs and Energy (BMWi) under grant number DLR 50 WM 1542 and DLR 50 WM 1762. T.Shinbrot acknowledges support from the US NSF, CBET award 1804286.

Author contributions

T.Steinpilz and F.J. designed and performed experiments and analysed the data. K.J. and L.B. wrote the code and performed the simulations. G.W., D.W. and J.T. conceived the research. T.Shinbrot contributed to the conception of research into electrostatic contributions to particle aggregation and to data analysis. All authors discussed the results and wrote the manuscript.

Competing interests

The authors declare no competing interests.

Additional information

Extended data is available for this paper at https://doi.org/10.1038/s41567-019-0728-9.

Supplementary information is available for this paper at https://doi.org/10.1038/s41567-019-0728-9.

Correspondence and requests for materials should be addressed to T.Steinpilz or G.W.

Peer review information *Nature Physics* thanks Katherine Follette and the other, anonymous, reviewer(s) for their contribution to the peer review of this work.

Reprints and permissions information is available at www.nature.com/reprints.

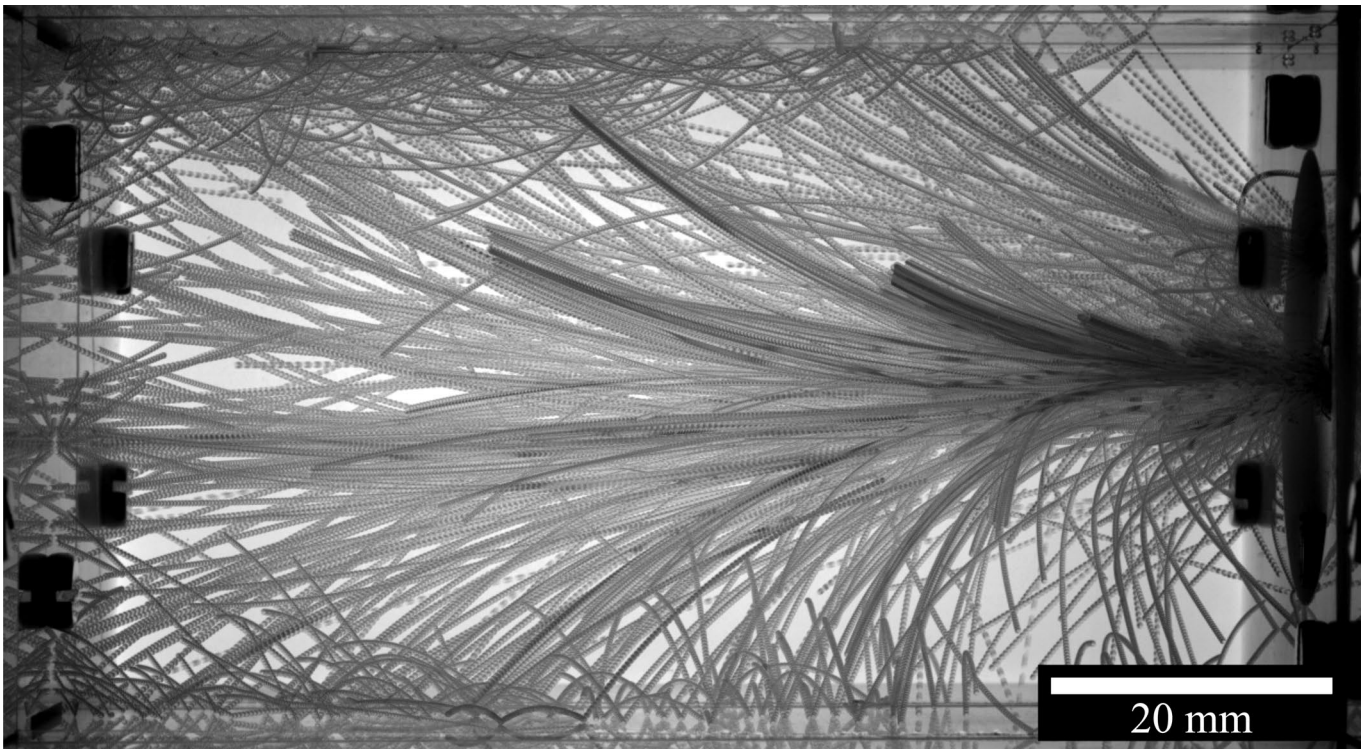

Extended Data Fig. 1 | Particle tracks in the electrical field. Tracks of individual charged grains between capacitor plates in microgravity. Particles enter from the shaker at the right. Tracks are made visible by superimposing a stack of 180 frames (consuming 1 s). Note rebounds are visible at the capacitor walls (top and bottom). For experiment parameters see Table 1.

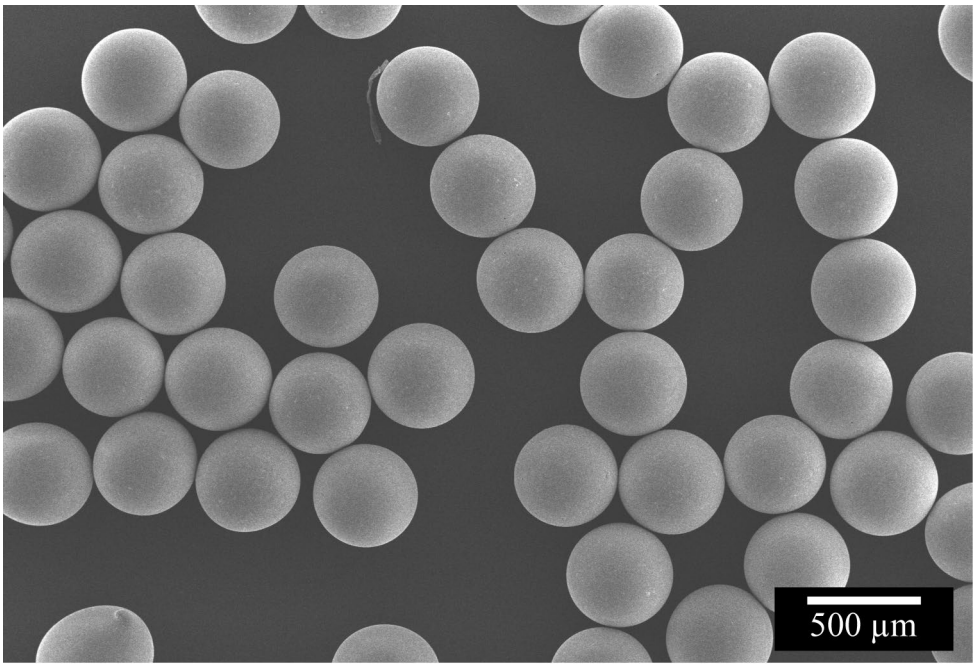

Extended Data Fig. 2 | Scanning electron microscope (SEM) image of sample particles. This image shows the glass particles of 434 μm diameter used in the experiments.

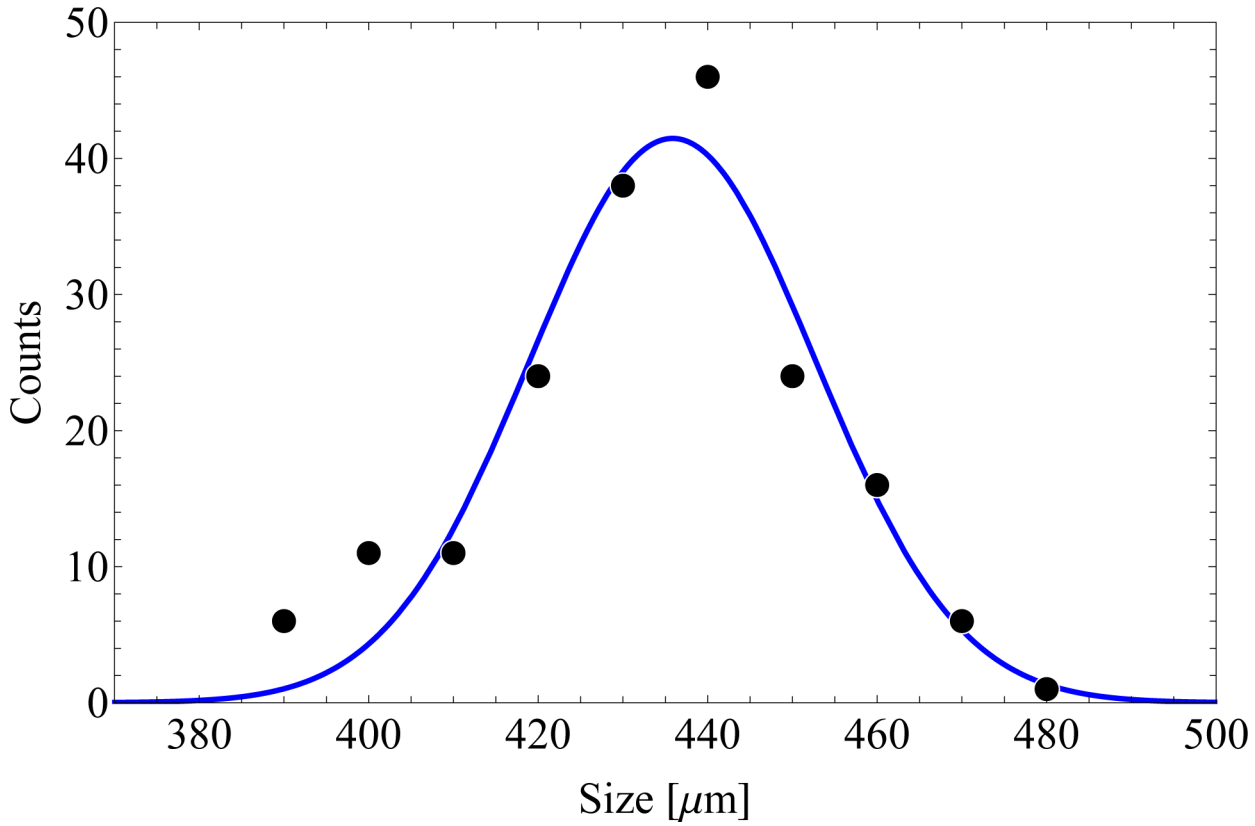

Extended Data Fig. 3 | Size distribution of the sample particles. The black dots show a histogram of the measured grain sizes of the glass particles used. The uncertainties in size determination of individual grains are 2 %. The blue line is a normal distribution fitted to the experimental data. From the fit we get an average grain diameter of 434 μm with the standard deviation of ± 17 μm.

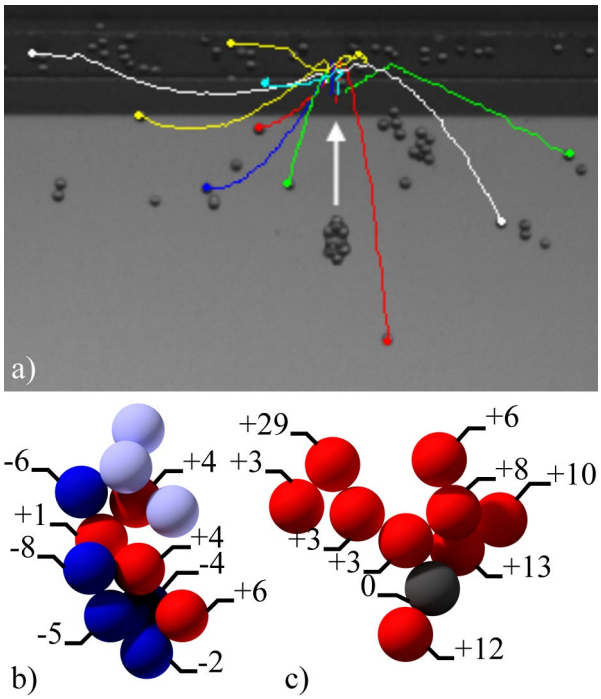

Extended Data Fig. 4 | Disintegration of charged aggregates. a: An aggregate below the white arrow collides with the top capacitor wall and fragments into individual grains. The image shows trajectories of the individual grains following disintegration and an overlay of the original aggregate. The acceleration of each particle in the capacitor field is used to determine the charges of all individual grain within the aggregate. **b**: Example of charges reconstructed from a disintegration event. Charges are expressed in 10^5 e. Unlabeled particles do not fragment adequately to establish their charge. The uncertainties due to the error of the trajectory fit, the mass distribution and the unknown position perpendicular to the observation plane are estimated to be 20 % of the net charge (experiment parameters in Table 1). **c**: Same as **b** but showing an aggregate that only consists of positive charges.

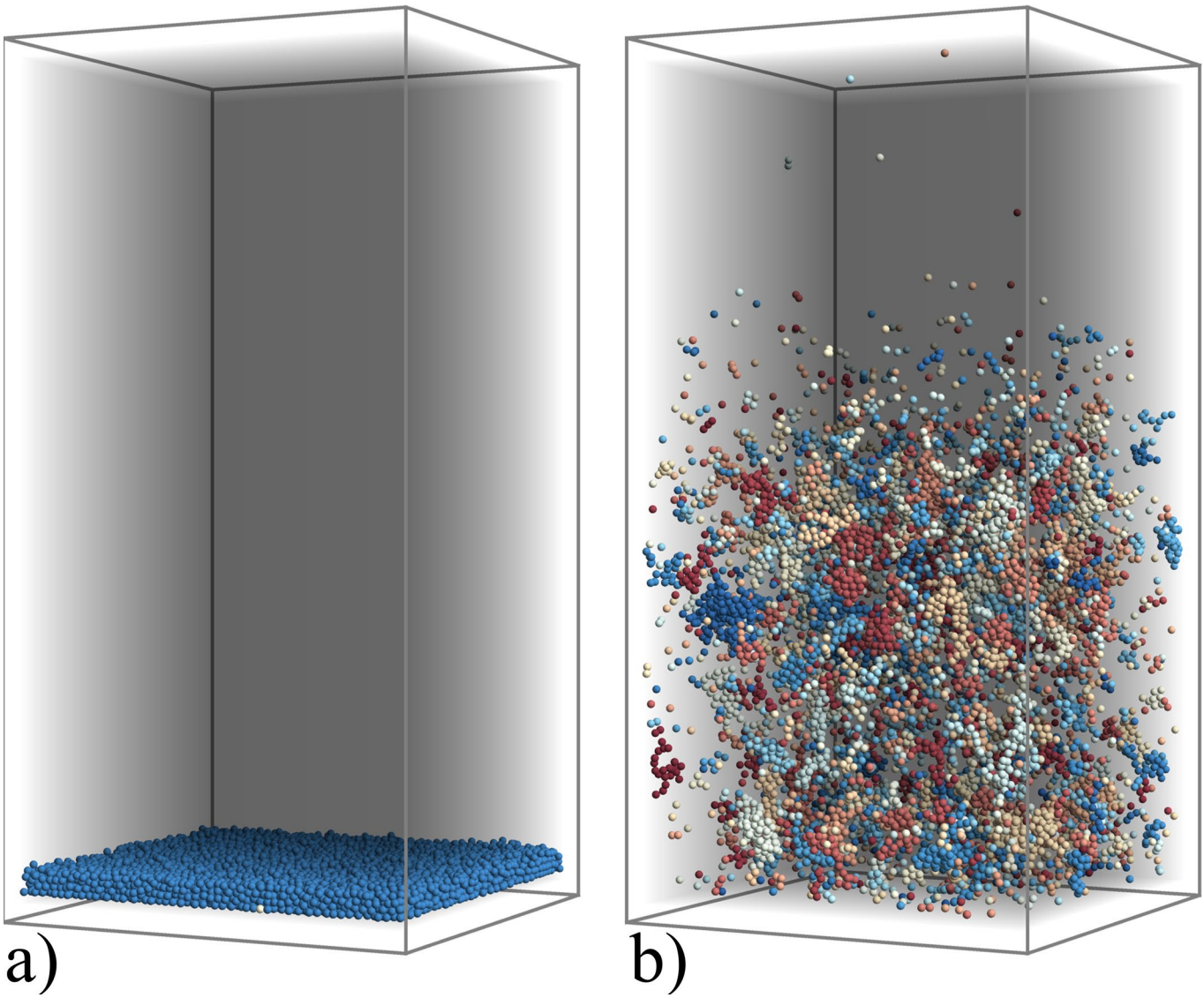

Extended Data Fig. 5 | Snapshots from the simulations. a: Initial configuration of the simulation. **b**: Simulated aggregates at a later time. Color is used to distinguish individual aggregates. All grains sticking to each other share the same color.

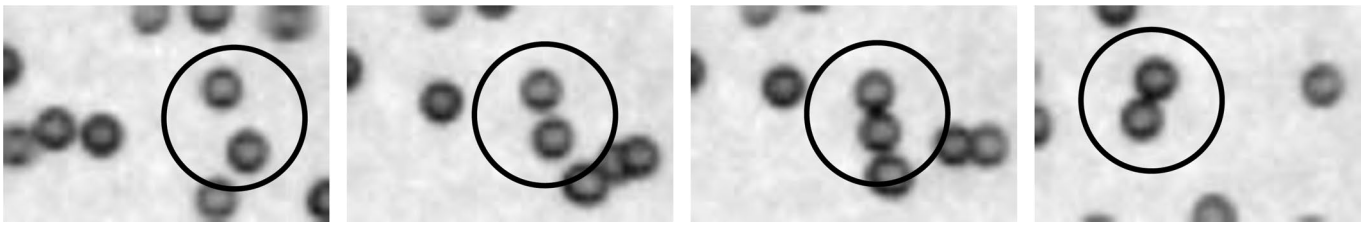

Extended Data Fig. 6 | Collision between two charged grains. Example of two 434 μm glass particles colliding at 5.4 mm s^{-1}. They collide, bounce off each other but collide a second time due to attractive Coulomb forces. They stick together, eventually.

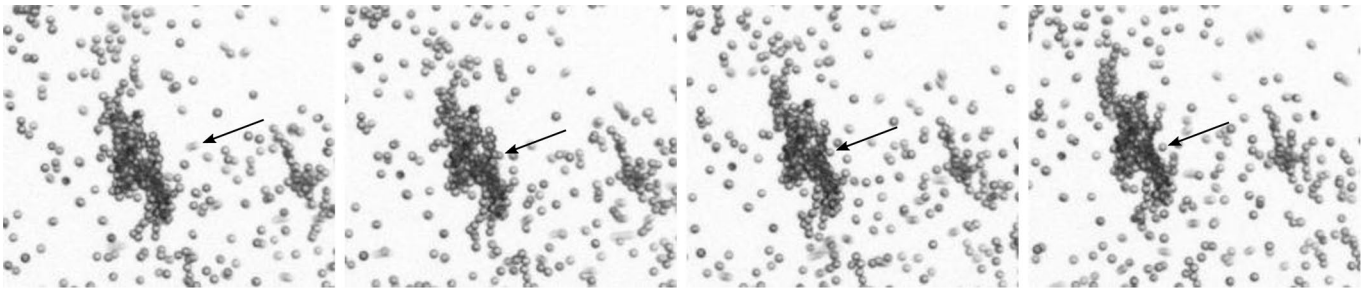

Extended Data Fig. 7 | Impact of individual grain into larger cluster. Marked by the arrow, an individual grain impacts a charged cluster at 0.13 m s^{-1}. The cluster only deforms but stays intact.

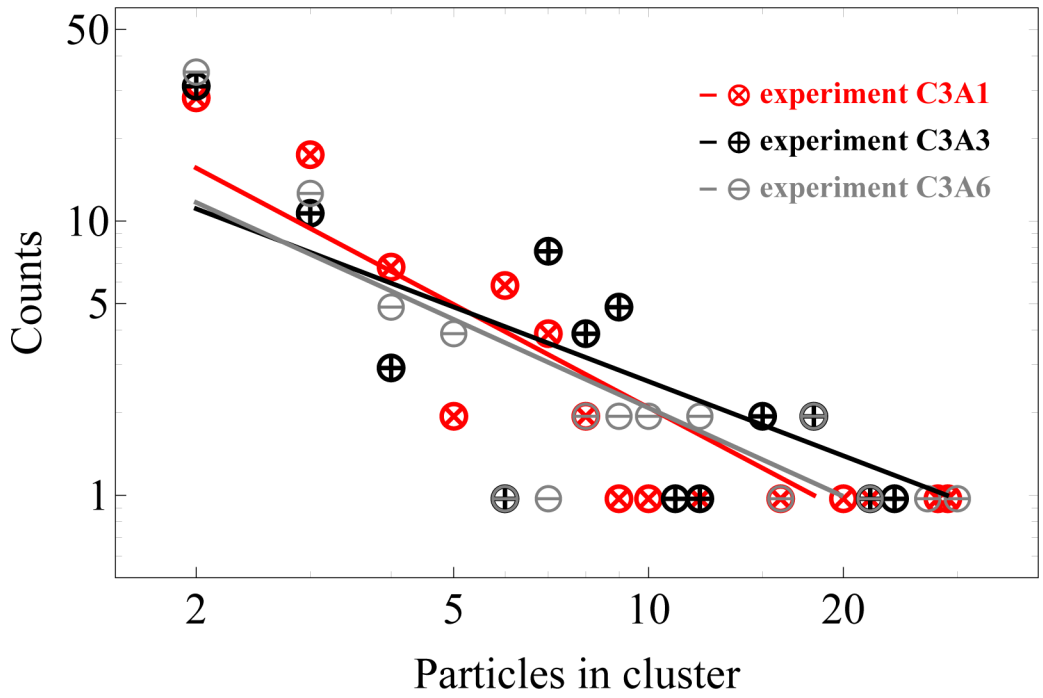

Extended Data Fig. 8 | Experimental raw data. Data of the 3 experimental trials added to generate the experimental data in Fig. 4. Shown are the measured numbers of clusters with a given particle number per cluster. The data are direct counts of grains and clusters and therefore have no error. Also added are power law fits to each data set. The slopes are -1.3, -0.9 and -1.1 for C3A1, C3A3 and C3A6, respectively.